Multiphoton ionization of H_2^+ in xuv laser pulses

Xiaoxu Guan,[1] Ethan B. Secor,[1] Klaus Bartschat,[1] and Barry I. Schneider[2]
[1]*Department of Physics and Astronomy, Drake University, Des Moines, Iowa 50311, USA*
[2]*Office of Cyberinfrastructure, National Science Foundation, Arlington, Virgina 22230, USA*
(Received 11 July 2011; published 26 September 2011)

We consider the ionization of the hydrogen molecular ion after one-, two-, and three-photon absorption over a large range of photon energies between 9 and 40 eV in the fixed-nuclei approximation. The temporal development of the system is obtained in a fully *ab initio* time-dependent grid-based approach in prolate spheroidal coordinates. The alignment dependence of the one-photon ionization amplitude is highlighted in the framework of time-dependent perturbation theory. For one-photon ionization as a function of the nuclear separation, the calculations reveal a significant minimum in the ionization probability. The suppressed ionization is attributed to a Cooper-type minimum, which is similar, but not identical, to the cancellation effect observed in photoionization cross sections of some noble-gas atoms. The effect of the nonspherical two-center Coulomb potential is analyzed. For two- and three-photon ionization, the angle-integrated cross sections clearly map out intermediate-state resonances, and the predictions of the current computations agree very well with those from time-independent calculations. The dominant emission modes for two-photon ionization are found to be very similar in both resonance and off-resonance regions.

DOI: 10.1103/PhysRevA.84.033420 PACS number(s): 33.80.Rv, 33.80.Wz, 31.15.A−

I. INTRODUCTION

As the simplest two-center one-electron molecular system, the hydrogen molecular ion provides an ideal prototype for diatomic molecules, and its history traces back to the dawn of quantum mechanics [1]. An early review of the analytical properties for solving the two-center one-electron Coulomb problem was given by Power [2]. Accurate numerical energies of the H_2^+ ion were tabulated by Madsen and Peek over a large range of internuclear separation [3].

With the ongoing rapid developments in intense femtosecond (fs) and attosecond (as) laser technologies and some new theoretical and computational approaches in full dimensionality, this simplest molecule, as well as its isotopes HD^+ and D_2^+, have served as a prime testing ground in recent years to explore fundamental processes such as the electron localization in dissociation channels [4,5], the double-slit interference effect [6–8], the mapping of vibrational wave packets followed by Coulomb explosion [9], and above-threshold dissociation [10,11] for laser wavelengths ranging from x-ray to infrared.

Due to the different characteristic time scales of the slower nuclear motion (fs scale) and faster electronic motion (as scale), most numerical simulations for molecular responses to temporal laser fields rely on the adiabatic Born-Oppenheimer (BO) approximation. Exercising caution, however, is necessary when these separated treatments for the electronic and nuclear degrees of freedom are applied in practice; for example, to near-threshold photoionization. The fixed-nuclei approximation (FNA), which neglects the coupling of the electronic states with the nuclear motion, has also been widely employed to study electronic ionization, including the interaction with 800 nm infrared pulses [12,13].

As discussed below, even within the FNA there still exist discrepancies between different numerical predictions for the differential cross sections (DCSs) and/or integral cross sections for multiphoton ionization. A striking example is the angular distribution for single-photon ionization of the aligned H_2^+ ion at the photon energy $\hbar\omega_0$ of 1.47 atomic units (a.u.) (40 eV). Very good agreement was achieved between results from time-dependent close-coupling (TDCC) treatments [14,15] in spherical coordinates and time-independent exterior complex scaling (ECS) calculations [16,17] for the parallel geometry of $\theta_N = 0^\circ$, where θ_N denotes the angle between the molecular axis $\boldsymbol{\zeta}$ and the polarization vector $\boldsymbol{\epsilon}$ (see Fig. 1). In other geometries with the alignment angle $\theta_N \neq 0^\circ$, the direct comparison of the TDCC and ECS results [14] is questionable. The published DCSs at $\theta_N = 30^\circ$ show noticeable (up to nearly 30%) differences between the predictions from these two calculations [14,17].

Another example is the angle-integrated cross section for two-photon ionization, obtained either in the TDCC approach or by well-established time-independent perturbation theory. The TDCC cross sections for two- and three-photon absorption [18] exhibit a significant sensitivity to the peak intensity of the laser field. The cross sections published in [18] are generally larger than the results of Plummer and McCann's Floquet calculations [19], even in the perturbative regime where one would expect the two sets of results to agree very well.

The present work also uses the FNA and describes improved calculations for one-photon, two-photon, and three-photon absorption by solving the time-dependent Schrödinger equation (TDSE) in two-center prolate spheroidal coordinates. The spatial "radial" (ξ) and "angular" (η) coordinates in elliptical coordinates are discretized through the finite-element discrete-variable representation (FE-DVR). Using the same discretization procedure but combining it with the time-independent ECS approach, Rescigno, McCurdy, and coworkers very recently considered the corresponding problem of steady-state one- and two-photon ionization of the H_2^+ ion [17,20].

There is little doubt that this relatively simple test case can also be solved in one-center spherical coordinates [14,15] and even in rectangular coordinates [21]. Nevertheless, grid-based approaches in prolate spheroidal coordinates have a number of appealing advantages to portray the response of diatomic

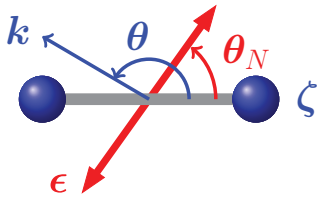

FIG. 1. (Color online) Definition of alignment angle θ_N and ejection angle θ of a photoelectron with momentum $\boldsymbol{k}$ for coplanar geometry in the molecular body frame.

molecules to laser pulses. Our long-term goal is to develop a time-dependent grid-based approach to handle the dynamical coupling between the electronic and nuclear motions in intense laser fields. This will allow for calculations to proceed beyond the limit of the FNA. As discussed in Ref. [17], it is very convenient to describe the coupling of nuclear and electronic motions in prolate spherical coordinates, since the internuclear separation appears in the electronic kinetic-energy part of the Hamiltonian as a scaling factor. Furthermore, all the potentials (nucleus-nucleus and nucleus-electron interactions) are diagonal with respect to the grid points in the DVR framework. In the time-independent scenario, the wave functions of bound and unbound states of the $H_2{}^+$ molecule can be produced with great accuracy in prolate spheroidal coordinates. Consequently, the cross sections for multiphoton ionization can be computed to a high degree of accuracy in the framework of lowest-order perturbation theory (LOPT) [22]. This provides a benchmark reference to gauge the results obtained from approximate treatments; for example, when using a linear combination of atomic-orbital wave functions for the initial state and/or two-body Coulomb functions centered at two individual nuclei for the final continuum states.

The remainder of this paper is organized as follows: After presenting our *ab initio* time-dependent formalism for multiphoton ionization in Sec. II, a time-dependent perturbative analysis in the framework of the first-order approximation for single-photon ionization is outlined in Sec. III. Results for angle-resolved differential and angle-integrated cross sections for one-, two-, and three-photon ionization are presented in Sec. IV. In that comparison, it becomes clear that some of the "different" results found in the literature differ due to varying, and often inconsistent, definitions used for the published cross sections. The paper concludes with a summary and an outlook in Sec. V.

II. *AB INITIO* TREATMENT OF MULTIPHOTON IONIZATION

At a fixed internuclear distance R, the wave function of the laser-driven $H_2{}^+$ system can be written as

$$\Psi(t) = \sum_{mij} b_{ij}^m(\xi,\eta,\varphi) C_{ij}^m(t) \tag{1}$$

in two-center prolate spheroidal coordinates. Here, the basis $b_{ij}^m(\xi,\eta,\varphi)$ is defined as

$$b_{ij}^m(\xi,\eta,\varphi) = \frac{1}{\sqrt{2\pi a^3\left(\xi_i^2-\eta_j^2\right)}} f_i(\xi) g_j(\eta) e^{im\varphi}, \tag{2}$$

where $a = R/2$ and m is the magnetic quantum number along the molecular axis. The above bases are normalized according to $\langle b_{ij}^m | b_{i'j'}^{m'} \rangle = \delta_{ii'}\delta_{jj'}\delta_{mm'}$, and $\{f_i(\xi)\}$ and $\{g_j(\eta)\}$ are the DVR bases for ξ and η, respectively. The configuration space is therefore discretized in the FE-DVR scheme. Reference [23] contains the technical details regarding the implementation of the appropriate boundary conditions in prolate spheroidal coordinates. The time-dependent expansion coefficients $\{C_{ij}^m(t)\}$ can be determined by solving the TDSE effectively through an iterative Lanzcos algorithm [24,25], either in imaginary time to obtain the initial state or in real time to propagate it.

The physical information about the ionization process by multiphoton absorption can be extracted through the projection of the wave packet, at the end of the time evolution, to the relevant continuum states. In prolate spheroidal coordinates, the partial-wave expansion of the continuum state $\Phi_{\boldsymbol{k}}^{(-)}(\boldsymbol{r})$ with momentum vector $\boldsymbol{k}$, satisfying the appropriate incoming boundary conditions, is written as

$$\Phi_{\boldsymbol{k}}^{(-)}(\boldsymbol{r}) = \frac{1}{k}\sum_{\ell m} i^\ell e^{-i\Delta_{m\ell}(k)} \mathcal{Y}_{\ell,m}^*(\boldsymbol{k}) \mathcal{Y}_{\ell,m}(k,\eta,\varphi) \Pi_{\ell,m}^{(k)}(\xi), \tag{3}$$

where $\mathcal{Y}_{\ell,m}$ and $\Pi_{\ell,m}^{(k)}(\xi)$ are the angular "spheroidal harmonics" and radial functions, respectively. $\Delta_{m\ell}(k)$ is the two-center Coulomb phase shift. It can be determined by normalizing the numerical solution to the known asymptotic behavior of the radial function,

$$\Pi_{\ell,m}^{(k)}(\xi) \to \frac{1}{\xi R}\sqrt{\frac{8}{\pi}} \sin\left(\frac{kR}{2}\xi + \frac{2}{k}\ln(kR\xi) - \frac{\ell\pi}{2} + \Delta_{|m|\ell}(k)\right) \tag{4}$$

as $\xi \to +\infty$. This normalizes $\Phi_{\boldsymbol{k}}^{(-)}(\boldsymbol{r})$ to a delta function in momentum space [i.e., $\langle \Phi_{\boldsymbol{k}}^{(-)} | \Phi_{\boldsymbol{k}'}^{(-)} \rangle = \delta(\boldsymbol{k}-\boldsymbol{k}')$].

Projecting the time-dependent wave function at the end of time evolution ($t = t_e$) onto the functions in Eq. (3) yields

$$\langle \Phi_{\boldsymbol{k}}^{(-)} | \Psi(t_e) \rangle = \frac{1}{k}\sum_{\ell m} (-i)^\ell e^{i\Delta_{m\ell}(k)} \mathcal{Y}_{\ell,m}(\boldsymbol{k}) \mathcal{F}_{\ell,m}(k), \tag{5}$$

where the partial-wave amplitude $\mathcal{F}_{\ell,m}(k)$ in the (ℓ,m) ionization channel is given by

$$\mathcal{F}_{\ell,m}(k) = \sum_{ij} \sqrt{a^3\left(\xi_i^2-\eta_j^2\right)} \Pi_{\ell,m}^{(k)}(\xi_i) \Xi_{\ell,m}^{(k)}(\eta_j) C_{ij}^m(t_e). \tag{6}$$

Here, $\Pi_{\ell,m}^{(k)}(\xi_i)$ and $\Xi_{\ell,m}^{(k)}(\eta_j)$ are the expansion coefficients of the "radial" and "angular" functions in terms of the normalized DVR $\{f_i(\xi)\}$ and $\{g_j(\eta)\}$ bases, respectively. This simple expression is a direct consequence of the FE-DVR representation. Consequently, the total ionization probability

($P_{\rm ion}$) at $t = t_e$ is obtained by collecting all the possible ionization events:

$$P_{\rm ion}(t_e) = \int_0^{+\infty} k^2 dk \int d\Omega |\langle \Phi_{\boldsymbol{k}}^{(-)} | \Psi(t_e)\rangle|^2 = \int d\boldsymbol{k} \frac{dP_{\rm ion}}{d\boldsymbol{k}}. \quad (7)$$

The probability density for ionization within the momentum-space volume $d\boldsymbol{k}$ is given by

$$\frac{dP_{\rm ion}}{d\boldsymbol{k}} = |\langle \Phi_{\boldsymbol{k}}^{(-)} | \Psi(t_e)\rangle|^2. \quad (8)$$

The probability density for ionization ($dP_{\rm ion}/d\Omega$) of the photoelectron scattered into the solid angle $d\Omega$ is

$$\frac{dP_{\rm ion}}{d\Omega} = \int k^2 dk \frac{dP_{\rm ion}}{d\boldsymbol{k}} = \int k^2 dk |\langle \Phi_{\boldsymbol{k}}^{(-)} | \Psi(t_e)\rangle|^2. \quad (9)$$

Equations (8) and (9) are general representations of the probability density for ionization (with respect to $d\boldsymbol{k}$) and the angular distribution (with respect to $d\Omega$) following N-photon absorption. They are valid not only for a weak but also for a strong field. On the other hand, if the laser field is sufficiently weak and the interaction between the laser pulse and the target does not cause significant depletion of the initial state, then the concept of cross sections (both angle-integrated total and angle-differential) is also applicable to describe the ionization process. As a consequence, it is possible to extract cross sections from a time-dependent scenario and make a meaningful comparison with the well-defined multiphoton-ionization cross section obtained by perturbation theory. In this case, the angular distribution in Eq. (9) can be converted to the differential cross section $d\sigma/d\Omega$ for N-photon absorption, which is given by

$$\frac{d\sigma^{(N)}}{d\Omega} = \left(\frac{\omega_0}{I_0}\right)^N \frac{1}{T_{\rm eff}^{(N)}} \frac{dP_{\rm ion}}{d\Omega} = \left(\frac{\omega_0}{I_0}\right)^N \frac{1}{T_{\rm eff}^{(N)}} \times \int dk \left| \sum_{\ell m} (-i)^\ell e^{i\Delta_{m\ell}(k)} \mathcal{Y}_{\ell,m}(\boldsymbol{k}) \mathcal{F}_{\ell,m}(k) \right|^2. \quad (10)$$

Here, ω_0 and I_0 are the central laser frequency and the peak intensity of the laser field, respectively. The essential ingredient is the so-called effective interaction time for N-photon ionization, $T_{\rm eff}^{(N)}$. If the pulse duration is τ and the envelope function $f(t)$ takes the frequently used sine-squared form of $f(t) = \sin^2(\pi t/\tau)$, then [26]

$$T_{\rm eff}^{(N)} = \int_0^\tau dt f^{2N}(t) = \frac{(4N-1)!!}{(4N)!!}\tau. \quad (11)$$

Note that the effective interaction time is much shorter than the pulse length (i.e., $T_{\rm eff}^{(N)} < \tau$) for all N-photon absorption cases. In particular,

$$T_{\rm eff}^{(1)} = \frac{3}{8}\tau, \quad T_{\rm eff}^{(2)} = \frac{35}{128}\tau, \text{ and } T_{\rm eff}^{(3)} = \frac{77}{3072}\tau, \quad (12)$$

respectively, for one-, two-, and three-photon absorption.

III. A PERTURBATIVE ANALYSIS OF ONE-PHOTON IONIZATION

The time-dependent LOPT is applicable to describe the ionization process through one-photon absorption if the external xuv laser field is relatively "weak." In this situation, the depletion of the initial state Φ_0 is neglected, and the time-dependent wave function of the system driven by a temporal perturbation $W(t)$ is written as

$$\Psi(t) = \Phi_0 e^{-iE_0 t} + \frac{1}{i}\sum_{n\geqslant 1} \int_0^t dt' W_{n0}(t') e^{i(E_n - E_0)t'} \Phi_n e^{-iE_n t}, \quad (13)$$

where $\{E_n, \Phi_n\}$ denotes the eigenenergies and wave functions of the field-free system and $W_{n0}(t') = \langle \Phi_n | W(t') | \Phi_0 \rangle$. The expansion in terms of the field-free excited eigenstates can be regrouped according to the magnetic quantum numbers of the final states. These can be $m = 0$ or $m = \pm 1$ in our case, respectively, depending upon the relative orientation of the $\boldsymbol{\epsilon}$ and $\boldsymbol{\zeta}$ axes. In the dipole-length form, the time-dependent perturbation due to the temporal electric field with amplitude E_A can be recast as

$$W(t) = E_A f(t) \cos(\omega_0 t) \left[\cos\theta_N r^{(0)} + \frac{1}{\sqrt{2}} \sin\theta_N e^{i\varphi_N} r^{(-1)} - \frac{1}{\sqrt{2}} \sin\theta_N e^{-i\varphi_N} r^{(+1)} \right].$$

Here, θ_N and φ_N denote, respectively, the polar and azimuthal angles of the polarization vector in the molecular frame. Furthermore, $r^{(0)} = z$ and $r^{(\pm 1)} = \mp(x \pm iy)/\sqrt{2}$. Equation (13) can then be rewritten as

$$\Psi(t) = \Phi_0 e^{-iE_0 t} + E_A \cos\theta_N \Phi^{(m=0)}(t) + \frac{1}{\sqrt{2}} E_A \sin\theta_N e^{i\varphi_N} \Phi^{(m=-1)}(t) + \frac{1}{\sqrt{2}} E_A \sin\theta_N e^{-i\varphi_N} \Phi^{(m=1)}(t). \quad (14)$$

The three components $\Phi^{(m=0,\pm 1)}(t)$ of the wave function are formally related to the unperturbed eigenstates through

$$\Phi^{(m)}(t) = \frac{1}{i}\sum_{n\geqslant 1} \left\langle \Phi_n^{(m)} \middle| r^{(m)} \middle| \Phi_0 \right\rangle \Phi_n^{(m)} \times \int_0^t dt' f(t') \cos(\omega_0 t') e^{i(E_n - E_0)t'} e^{-iE_n t}. \quad (15)$$

From Eqs. (14) and (15), the dependence of the wave function on the amplitude of the electric field (E_A) and the orientation (θ_N,φ_N) can be completely factored out in the limit of LOPT. After the separation, the resulting components introduced in Eq. (15) only depend on the laser parameters through the temporal function $f(t)$, but they are independent of E_A and the orientation angles. Note that this conclusion not only holds for one-electron but also for multielectron atoms and molecules.

The ionization amplitude can then be calculated by projecting onto the ungerade continuum state ($\Phi_{\boldsymbol{k}}^{u}$). We obtain

$$\begin{aligned}\left\langle \Phi_{\boldsymbol{k}}^{u}\middle|\Psi(t)\right\rangle = {} & E_A\cos\theta_N P_{\Sigma_u}^{(m=0)}(\boldsymbol{k}) \\ & + \frac{1}{\sqrt{2}}E_A\sin\theta_N e^{i\varphi_N} P_{\Pi_u}^{(m=-1)}(\boldsymbol{k}) \\ & + \frac{1}{\sqrt{2}}E_A\sin\theta_N e^{-i\varphi_N} P_{\Pi_u}^{(m=1)}(\boldsymbol{k}), \end{aligned} \tag{16}$$

where $\boldsymbol{k}$ is the momentum of the photoelectron, $P_{\Sigma_u}^{(m=0)}(\boldsymbol{k}) = \langle\Phi_{\boldsymbol{k}}^{u}|\Phi^{(m=0)}(t)\rangle$, and $P_{\Pi_u}^{(m=\pm1)}(\boldsymbol{k}) = \langle\Phi_{\boldsymbol{k}}^{u}|\Phi^{(m=\pm1)}(t)\rangle$, respectively. Comparison with the general *ab initio* formalism given in Eq. (5) reveals that

$$\frac{1}{k}\sum_{\ell}(-i)^l e^{i\Delta_{0\ell}(k)}\mathcal{Y}_{\ell,0}(\boldsymbol{k})\mathcal{F}_{\ell,0}(k) = E_A\cos\theta_N P_{\Sigma_u}^{(m=0)}(\boldsymbol{k}), \tag{17}$$

and

$$\begin{aligned}&\frac{1}{k}\sum_{\ell}(-i)^{\ell} e^{i\Delta_{1\ell}(k)}\mathcal{Y}_{\ell,\pm1}(\boldsymbol{k})\mathcal{F}_{\ell,\pm1}(k) \\ &\quad = \frac{1}{\sqrt{2}}E_A\sin\theta_N e^{\mp i\varphi_N} P_{\Pi_u}^{(m=\pm1)}(\boldsymbol{k}) \end{aligned} \tag{18}$$

for the cases in which the LOPT is a suitable approximation.

This indicates that only $\mathcal{F}_{\ell,m}(k)$ depends on E_A and the orientation (θ_N,φ_N), and it suggests that another separation may be carried out. We therefore define

$$\mathcal{F}_{\ell,0}(k) = E_A\cos\theta_N F_{\ell,0}(k) \tag{19}$$

and

$$\mathcal{F}_{\ell,\pm1}(k) = E_A\frac{1}{\sqrt{2}}\sin\theta_N e^{\mp i\varphi_N} F_{\ell,\pm1}(k), \tag{20}$$

in which the reduced momentum distributions $F_{\ell,m}(k)$ no longer contain any dependence on the laser parameters (E_A,θ_N,φ_N). This can be understood from the fact that, in LOPT, the expansion coefficients $C_{ij}^{M}(t)$ are proportional to $E_A\cos\theta_N$ or $E_A\sin\theta_N e^{\pm i\varphi_N}$, depending on $m=0$ or $m=\pm1$. We have $\mathcal{F}_{\ell,0}(k) = E_A F_{\ell,0}(k)$ for the parallel geometry ($\theta_N = 0^\circ$), while $\mathcal{F}_{\ell,\pm1}(k) = E_A e^{\mp i\varphi_N} F_{\ell,\pm1}(k)/\sqrt{2}$ for the perpendicular case ($\theta_N = 90^\circ$). As a consequence of the above considerations, for an arbitrary geometry ($0^\circ \leqslant \theta_N \leqslant 90^\circ$) and arbitrary angle φ_N in the region $[0,2\pi]$,

$$|\mathcal{F}_{\ell,0}(k,\theta_N,\varphi_N)|^2 = \cos^2\theta_N|\mathcal{F}_{\ell,0}(k,\theta_N=0^\circ,\varphi_N)|^2 \tag{21}$$

and

$$|\mathcal{F}_{\ell,\pm1}(k,\theta_N,\varphi_N)|^2 = \sin^2\theta_N|\mathcal{F}_{\ell,\pm1}(k,\theta_N=90^\circ,\varphi_N)|^2. \tag{22}$$

Using Eqs. (21) and (22) in the LOPT scheme, the differential cross section for one-photon ionization can be written as

$$\begin{aligned}\frac{d\sigma}{d\Omega} = {} & \frac{\omega_0}{I_0}\frac{1}{T_{\rm eff}^{(1)}}\int_0^{k_{\max}} dk\Bigg|\cos\theta_N\sum_{\ell}(-i)^{\ell}e^{i\Delta_{0\ell}(k)}\mathcal{Y}_{\ell,0}(\boldsymbol{k})F_{\ell,0}(k) \\ & + \frac{1}{\sqrt{2}}\sin\theta_N e^{-i\varphi_N}\sum_{\ell}(-i)^{\ell}e^{i\Delta_{1\ell}(k)}\mathcal{Y}_{\ell,-1}(\boldsymbol{k})F_{\ell,-1}(k) \\ & + \frac{1}{\sqrt{2}}\sin\theta_N e^{i\varphi_N}\sum_{\ell}(-i)^{l}e^{i\Delta_{1\ell}(k)}\mathcal{Y}_{\ell,1}(\boldsymbol{k})F_{\ell,1}(k)\Bigg|^2. \end{aligned} \tag{23}$$

A similar expression for the DCS was used in Ref. [27] in the "weak-field" limit, which is essentially a first-order approximation. The total angle-integrated cross section is therefore given by

$$\begin{aligned}\sigma(\theta_N) = {} & \frac{\omega_0}{I_0}\frac{P_{\rm ion}(\theta_N)}{T_{\rm eff}^{(1)}} \\ = {} & \frac{\omega_0}{I_0}\frac{1}{T_{\rm eff}^{(1)}}\int_0^{k_{\max}} dk\Big\{\cos^2\theta_N|F_{\ell,0}(k)|^2 \\ & + \sin^2\theta_N[|F_{\ell,-1}(k)|^2 + |F_{\ell,1}(k)|^2]\Big\}. \end{aligned} \tag{24}$$

The ionization probability at the end of pulse is given by

$$\begin{aligned}P_{\rm ion}(\theta_N) = \int_0^{k_{\max}} dk\Big\{&\cos^2\theta_N|F_{l,0}(k)|^2 + \sin^2\theta_N[|F_{\ell,-1}(k)|^2 \\ & + |F_{\ell,1}(k)|^2]\Big\}. \end{aligned} \tag{25}$$

The above ionization probability can be rewritten as

$$P_{\rm ion}(\theta_N) = \cos^2\theta_N P_{\rm ion}^{\parallel} + \sin^2\theta_N P_{\rm ion}^{\perp}, \tag{26}$$

where $P_{\rm ion}^{\parallel}$ and $P_{\rm ion}^{\perp}$ are the ionization probabilities

$$P_{\rm ion}^{\parallel} = \int_0^{k_{\max}} dk|F_{\ell,0}(k)|^2 \tag{27}$$

in the parallel geometry and

$$P_{\rm ion}^{\perp} = \int_0^{k_{\max}} dk[|F_{\ell,-1}(k)|^2 + |F_{\ell,1}(k)|^2] \tag{28}$$

in the perpendicular geometry, respectively. Equation (26) is the same as Eq. (31) of Ref. [28], which was obtained for a time-independent scenario. This demonstrates that the ionization events are rotationally symmetric with respect to the molecular axis. Physically, in LOPT, the ionization probability and therefore the integral cross section for an arbitrary geometry (θ_N,φ_N) can be simply obtained as a linear combination of ionization probabilities in the parallel and perpendicular geometries, where the weighting factors are simple trigonometric functions. Equations (23) and (24) reveal how the DCS depends on the orientation of the linear polarization axis through the angles θ_N and φ_N. Averaging over the entire solid angle (4π), the DCS for unpolarized laser fields is given by

$$\frac{d\sigma_{\rm av}}{d\Omega} = \frac{1}{3}\frac{d\sigma^{(\parallel)}}{d\Omega} + \frac{2}{3}\frac{d\sigma^{(\perp)}}{d\Omega}. \tag{29}$$

Here, $d\sigma^{(\parallel)}/d\Omega$ and $d\sigma^{(\perp)}/d\Omega$ are the differential cross sections in the parallel and perpendicular geometries, respectively. This also means that $\sigma_{\rm av} = [\sigma^{(\parallel)} + 2\sigma^{(\perp)}]/3$ for the total integral cross sections. The factors of 1/3 and 2/3 are the statistical weights of the Σ_u and Π_u symmetries.

For one-photon ionization of the H_2^+ ion, it is possible to use the standard time-independent formalism to compute the DCS. For a given photon energy ω_0, the momentum $\boldsymbol{k}$ of the photoelectron, and the polarization axis ($\boldsymbol{\epsilon}$), the time-independent DCS in the length gauge is given by

$$\frac{d\sigma}{d\Omega} = 4\pi^2\alpha\omega_0 k|\langle\Phi_{\boldsymbol{k}}^{(-)}(\boldsymbol{r})|\boldsymbol{\epsilon}\cdot\boldsymbol{r}|\Phi_0(\boldsymbol{r})\rangle|^2, \tag{30}$$

where $\alpha \approx 1/137$ is the fine structure constant. The continuum states are again normalized according to $\langle\Phi_{\boldsymbol{k}}^{(-)}|\Phi_{\boldsymbol{k}'}^{(-)}\rangle =$

TABLE I. Ionization probabilities for the aligned H_2^+ ion. $P_{\rm ion}^{(a)}$ and $P_{\rm ion}^{(b)}$ are the ionization probabilities at the end of the laser pulse, obtained from the *ab initio* calculation and Eq. (26), respectively. A sine-squared laser pulse with ten optical cycles at the central photon energy of 1.47 a.u. (40 eV) was used. [n] means 10 raised to the nth power.

θ_N	$P_{\rm ion}^{(a)}$	$P_{\rm ion}^{(b)}$	$P_{\rm ion}^{(a)}$	$P_{\rm ion}^{(b)}$
	10^{12} W/cm^2		10^{13} W/cm^2	
0°	2.330[−6]		2.330[−5]	
30°	9.987[−6]	9.987[−6]	9.987[−5]	9.985[−5]
60°	2.530[−5]	2.530[−5]	2.530[−4]	2.530[−4]
90°	3.296[−5]		3.295[−4]	
	10^{14} W/cm^2		10^{15} W/cm^2	
0°	2.327[−4]		2.304[−3]	
30°	9.980[−4]	9.965[−4]	9.911[−3]	9.770[−3]
60°	2.526[−3]	2.524[−3]	2.484[−2]	2.470[−2]
90°	3.288[−3]		3.217[−2]	

$\delta(\boldsymbol{k}-\boldsymbol{k}')$ in momentum space. The prolate spheroidal coordinate system enables a very accurate treatment of both the initial bound and final continuum state, thus providing the opportunity to carry out a self-consistent examination of the DCSs from both the time-dependent and time-independent formulations.

IV. RESULTS AND DISCUSSION

A. Energy levels of the H_2^+ ion

The FE-DVR technique in prolate spheroidal coordinates developed in this work is a high-precision representation for one-electron, two-center problems. The ξ coordinate was typically truncated at $\xi_{\rm max} = 400$. However, for pulses as long as 20 fs, a much larger extension with $\xi_{\rm max} = 1020$ was employed. The ξ coordinate was decomposed into 2 finite elements in the inner region ($1 < \xi \leqslant 5$) and 78–198 finite elements (depending on $\xi_{\rm max}$) in the outer region ($5 \leqslant \xi \leqslant \xi_{\rm max}$). Each element contained 10 Gauss-Radau or Gauss-Lobatto points. The η coordinate for these calculations is discretized by introducing 15 Gauss-Legendre points in a single finite element. At the equilibrium distance of $R = 2.0$ bohr, the electronic energy of the initial $^2\Sigma_g^+$ state obtained by solving the TDSE in imaginary time was $-1.102\,634\,214\,489\,42$ a.u., in excellent agreement with the benchmark value of Madsen and Peek [3].

B. One-photon ionization

In Table I, the applicability of Eq. (26) is examined at a variety of peak intensities from "weak" field (10^{12} W/cm^2) to "strong" field (10^{15} W/cm^2) for a fixed ten-cycle pulse. At a sufficiently weak field, the ionization probability follows the prediction of Eq. (26) very accurately. When the peak intensity of the field increases, the agreement between Eq. (26) and the *ab initio* calculation gradually deteriorates. The validity of Eq. (26) relies on the assumption of a negligible depletion of the initial state at the end of the pulse in lowest-order perturbation theory.

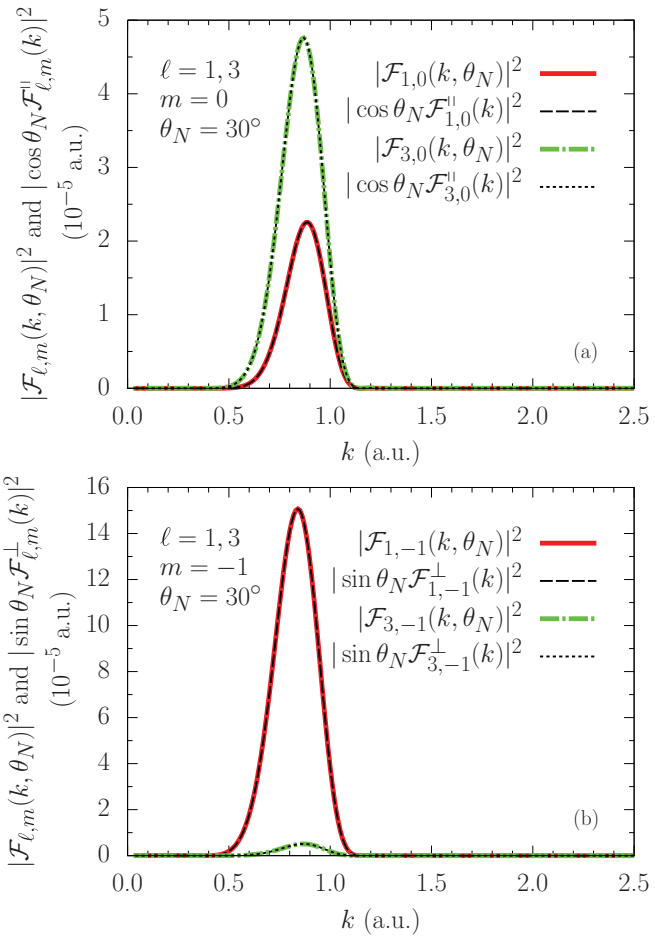

FIG. 2. (Color online) (a) Functions $|\mathcal{F}_{\ell,m}(k,\theta_N)|^2$ and $|\cos\theta_N \mathcal{F}^{\parallel}_{\ell,m}(k)|^2$ for $m = 0$ [cf. Eq. (21)]. (b) Functions $|\mathcal{F}_{\ell,m}(k,\theta_N)|^2$ and $|\sin\theta_N \mathcal{F}^{\perp}_{\ell,m}(k)|^2$ for $m = -1$ [cf. Eq. (22)]. $\ell = 1$, 3 and $\theta_N = 30°$ in both (a) and (b). A laser pulse with sine-squared envelope, a peak intensity of 10^{13} W/cm^2, and a central photon energy of 1.47 a.u. was used. The pulse time duration is 10 optical cycles.

Figure 2 shows the numerical results for the cases $m = 0$ and $m = -1$ with $\varphi_N = 0°$, thereby illustrating the validity of Eqs. (21) and (22) at the photon energy of 1.47 a.u. and a peak intensity of 10^{13} W/cm^2. The excellent agreement with the scaling rules established in Eqs. (21) and (22) indicates that the laser field of 10^{13} W/cm^2 essentially falls into the weak-field regime for this photon energy. The figure also shows the relative contributions from different ionization channels. For the aligned molecule with $0° < \theta_N < 90°$, final continuum states of the $^2\Sigma_u$ and $^2\Pi_u$ symmetries are accessible. For the $^2\Sigma_u$ channel, the contribution to the ionization probability from $(\ell,m) = (3,0)$ is larger than that from (1,0), while for the $^2\Pi_u$ channel, the contribution from $(1, -1)$ dominates significantly over that from $(3, -1)$. Note that all the contributions from different ionization channels are centered at the momentum of 0.86 a.u. Correspondingly, the kinetic energy of the photoelectron is 0.367 a.u. ($\simeq$10 eV). This is equivalent to the available excess energy after the absorption of one photon with energy 1.47 a.u.

Figure 3 shows the angle-resolved differential cross sections at the photon energy of 1.47 a.u. The DCSs in the

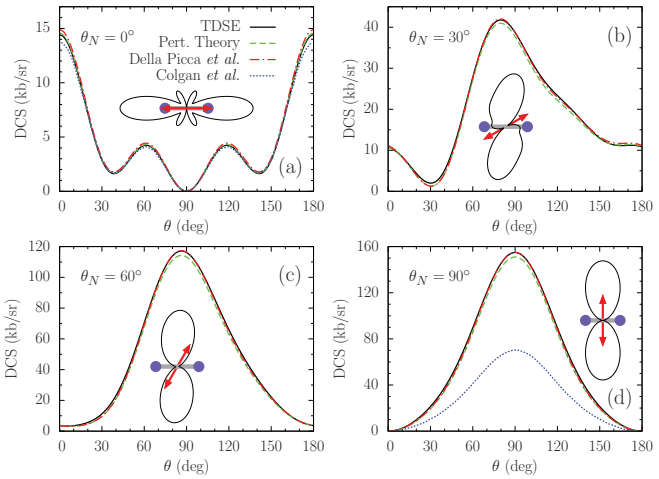

FIG. 3. (Color online) The angle-resolved differential cross section of the aligned H_2^+ ion in the molecular body frame at the central photon energy of 1.47 a.u. The alignment angle θ_N and ejection angle θ are defined in Fig. 1. The present time-dependent calculations (TDSE, solid line) were performed with a sine-squared envelope of the laser pulse at a peak intensity of 10^{13} W/cm^2 and a time duration of 10 optical cycles. The dashed lines represent the current time-independent results from perturbation theory, while the dot-dashed lines correspond to the time-independent results in the prolate spheroidal coordinates of Della Picca *et al.* [29] ($\theta_N = 0°$ and 90°) and [30] ($\theta_N = 30°$ and 60°). Finally, the dotted lines (only for $\theta_N = 0°$ and $\theta_N = 90°$) represent the TDCC results obtained in one-center spherical coordinates [15]. The angular distribution patters shown in polar coordinates correspond to the present time-dependent results. The nuclear separation distance is 2.0 bohr, and 1 kb $= 10^{-21}$ cm^2.

time-dependent treatment were extracted by using a 10-cycle laser pulse of peak intensity 10^{13} W/cm^2. The current time-dependent and time-independent DCSs are in excellent agreement with each other. Results from another recent calculation by Della Picca *et al.* [29,30] who applied the same time-independent formalism as our Eq. (30), are also shown. Their DCSs strongly support the present calculations. TDCC results [15] are shown in Fig. 3, whenever such a comparison is possible ($\theta_N = 0°$ and 90°).

The DCSs in the parallel geometry are all in excellent agreement with each other, but the TDCC result in the perpendicular geometry is significantly smaller than ours. The difference between the two calculations is partly due to the fact that the TDCC results of Ref. [15], both in the parallel and perpendicular geometries, are unweighted. In Ref. [14], on the other hand, the TDCC result for the DCS in the parallel geometry was weighted, while the DCS in the perpendicular geometry was still unweighted. This will be discussed in more detail with Eq. (34) below.

For the intermediate cases, the three sets of available results; namely, the TDCC results of Ref. [14], the DCSs predicted in Refs. [16,17], and our present numbers, are not directly comparable. Although by no means obvious, the present investigations revealed that apparently different definitions were used for the angle-resolved differential cross sections. In Ref. [14], the Σ_u amplitude was multiplied by a factor of $\sqrt{1/3}$, while no factor was used for the Π_u amplitude. On the other hand, both the Σ_u and Π_u amplitudes were premultiplied by $\sqrt{1/3}$ and $\sqrt{2/3}$, respectively, in the ECS calculations [16,17].

We will now demonstrate that, for a fixed alignment angle θ_N, there exists a simple relationship between the DCSs for two particular emission angles, $\theta = 0°$ and 90°. For a given emission angle $\Omega = (\theta,\varphi)$ of the photoelectron we have from Eq. (30) that

$$\frac{d\sigma^{(\theta_N)}}{d\Omega} = \sin^2\theta_N \frac{d\sigma^{(\perp)}}{d\Omega} + \cos^2\theta_N \frac{d\sigma^{(\parallel)}}{d\Omega} + 2\sin\theta_N\cos\theta_N \,\mathrm{Re}\left[\langle\Phi_{\boldsymbol{k}}^{(-)}|x|\Phi_0\rangle\langle\Phi_{\boldsymbol{k}}^{(-)}|z|\Phi_0\rangle\right]. \tag{31}$$

Unlike the total cross section (or the ionization probability), a simple decomposition of the DCS in terms of parallel and perpendicular components does not exist due to the interference term. However, this term vanishes at $\theta = 0°$ and $\theta = 90°$ (with respect to the molecular axis) where the DCSs are simply given as a linear combination of the DCSs in the parallel and perpendicular geometries. Specifically,

$$\frac{d\sigma^{(\theta_N)}}{d\Omega} = \sin^2\theta_N \frac{d\sigma^{(\perp)}}{d\Omega} + \cos^2\theta_N \frac{d\sigma^{(\parallel)}}{d\Omega}. \tag{32}$$

The ratio between the DCSs at $\theta = 90°$ and 0°,

$$\mathcal{D}(\theta_N) \equiv \frac{\mathrm{DCS}(90°,\theta_N)}{\mathrm{DCS}(0°,\theta_N)} = \frac{\sin^2\theta_N \mathrm{DCS}^{(\perp)}(90°) + \cos^2\theta_N \mathrm{DCS}^{(\parallel)}(90°)}{\sin^2\theta_N \mathrm{DCS}^{(\perp)}(0°) + \cos^2\theta_N \mathrm{DCS}^{(\parallel)}(0°)}, \tag{33}$$

is readily obtained from the relevant DCSs in the parallel and perpendicular geometries. This provides a convenient consistency test for the correctness of the calculated—and measured—DCSs in arbitrary alignment geometries.

In the above equations, we did not explicitly introduce the statistical weights for parallel (1/3) and perpendicular (2/3) geometries. Numerical tests confirmed that the present results satisfy the requirement of Eq. (32). In some references [16,17], the statistical weights were explicitly multiplied into the results for the DCSs. This "weighted" DCS,

$$\frac{d\widetilde{\sigma}^{(\parallel)}}{d\Omega} = \frac{1}{3}\frac{d\sigma^{(\parallel)}}{d\Omega} \quad \text{and} \quad \frac{d\widetilde{\sigma}^{(\perp)}}{d\Omega} = \frac{2}{3}\frac{d\sigma^{(\perp)}}{d\Omega}, \tag{34}$$

was apparently shown in Fig. 5 of Ref. [16] for $\theta_N = 0°$ and 90°. Comparison of the "weighted" DCSs of the current calculations and those of Ref. [16] show fairly satisfactory agreement.

In the general case (e.g., at $\theta_N = 30°$ or 60°), we noticed that the published results of Ref. [16] cannot be represented by Eq. (32), even after multiplying them by an overall factor independent of the emission angle. The DCS results in Ref. [16] are apparently not based on the standard definition of angle-resolved differential cross sections. Further numerical "experiments" then showed that replacing $\boldsymbol{\epsilon}\cdot\boldsymbol{r} = z\cos\theta_N + x\sin\theta_N$ by $\sqrt{1/3}\,z\cos\theta_N + \sqrt{2/3}\,x\sin\theta_N$ produced a "modified" DCS, $d\widetilde{\sigma}/d\Omega$, given by

$$\frac{d\widetilde{\sigma}}{d\Omega} = 4\pi^2\alpha\omega_0 k|\langle\Phi_{\boldsymbol{k}}^{(-)}(\boldsymbol{r})|\sqrt{\frac{1}{3}}z\cos\theta_N + \sqrt{\frac{2}{3}}x\sin\theta_N|\Psi_0(\boldsymbol{r})\rangle|^2. \tag{35}$$

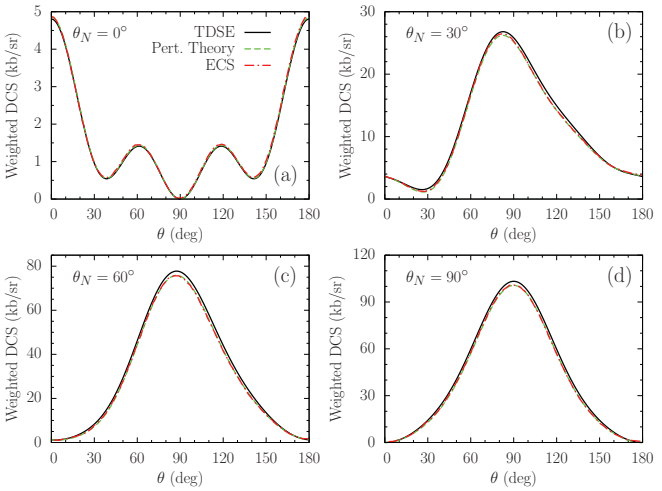

FIG. 4. (Color online) The "weighted" angle-resolved differential cross section [cf. Eq. (35)] of the aligned H_2^+ ion at the central photon energy of 1.47 a.u. The solid lines (TDSE) represent the current time-dependent calculations with a sine-squared laser pulse of peak intensity 10^{13} W/cm^2 and a time duration of 10 optical cycles. The dashed lines are the current time-independent results from perturbation theory, and the dot-dashed lines correspond to the time-independent ECS results in prolate spheroidal coordinates [17]. The nuclear separation distance is 2.0 bohr.

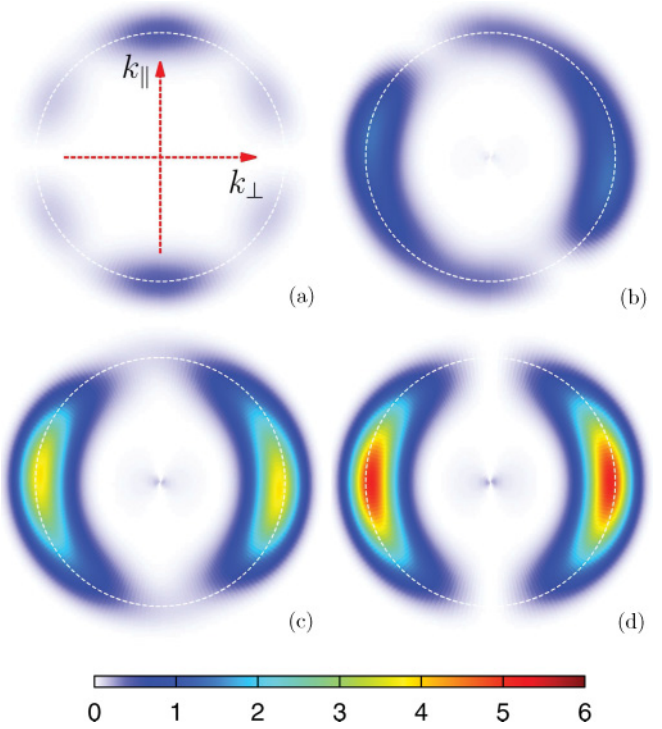

FIG. 5. (Color online) Single-photon ionization probability density $dP_{\rm ion}/d\boldsymbol{k}$ in the $\boldsymbol{\epsilon}$-$\boldsymbol{\zeta}$ plane for various alignment angles θ_N: (a) 0°, (b) 30°, (c) 60°, and (d) 90°. The molecular axis is orientated vertically. $k_\parallel$ and $k_\perp$ are the parallel and perpendicular components of momentum $\boldsymbol{k}$, respectively, with respect to the molecular axis. The laser parameters are the same as in Fig. 3. The classical momentum is shown as the dashed circle with a momentum radius of 0.86 a.u. The linear-scale color bar is given in 10^{-4} per momentum in a.u.

This is equivalent to introducing additional factors of $\sqrt{1/3}$ and $\sqrt{2/3}$ into the Σ_u and Π_u amplitudes. As shown in Fig. 4, excellent agreement between our "modified" results and those reported in Refs. [16,17] is obtained. A feature of the "modified" DCS is that the resulting total cross sections, obtained after integrating over the emission angles and averaging over the alignment orientations, have the statistical weight factors of 1/3 and 2/3 automatically built in. However, the usefulness of the definition for intermediate cases, including $\theta_N = 30°$ or 60°, is specious and has resulted in significant confusion in the literature.

Figure 5 exhibits the momentum density of the ionization probability, $dP_{\rm ion}/d\boldsymbol{k}$, in terms of the parallel ($k_\parallel$) and perpendicular ($k_\perp$) momentum components, in the plane formed by the molecular axis and the polarization vector. Essentially, $dP_{\rm ion}/d\boldsymbol{k}$ is the two-dimensional representation of the angular distributions. Even at $\theta_N = 30°$, the angular distribution is strongly bent toward the perpendicular direction. For $\theta_N \geqslant 30°$, therefore, the photoelectron is predominantly emitted along the direction of the polarization vector. The mode of parallel emission is only important close to the parallel geometry for one-photon ionization.

Figure 5 reveals that, in the parallel geometry ($\theta_N = 0°$), the photoelectron cannot be ejected in the plane perpendicular to the molecular axis. This rigorous selection rule demonstrates that the emission mode in the perpendicular plane is strictly forbidden in the parallel geometry. This can be understood from the nodal structure of the final continuum state $\Phi_{\boldsymbol{k}}^{(-)}(\boldsymbol{r})$ with $m = 0$ and ungerade parity. For the momentum $\boldsymbol{k}$ lying in that normal plane, we have $\Phi_{-\boldsymbol{k}}^{(-)}(\boldsymbol{r}) = \Phi_{\boldsymbol{k}}^{(-)}(-\boldsymbol{r}) = -\Phi_{\boldsymbol{k}}^{(-)}(\boldsymbol{r})$. At the same time, $\Phi_{-\boldsymbol{k}}^{(-)}(\boldsymbol{r}) = \Phi_{\boldsymbol{k}}^{(-)}(\boldsymbol{r})$ since there is no azimuthal-angle dependence for the Σ continuum state [cf. Eq. (3)]. Consequently, the normal plane is a nodal plane on which $\Phi_{\boldsymbol{k}}^{(-)}(\boldsymbol{r}) = 0$.

In the perpendicular geometry ($\theta_N = 90°$) a different emission mode is observed. Due to the symmetry in the Π_u channel, the electron once again cannot be ejected along the direction of the molecular axis in the normal geometry. This emission pattern is different from that in the parallel geometry. For $\theta_N = 0°$, the forbidden directions of emission form a plane normal to the $\boldsymbol{\epsilon}$ (or $\boldsymbol{\zeta}$) axis. In the case of $\theta_N = 90°$, however, the emission mode of the photoelectron is forbidden only along a particular line; namely, the $\boldsymbol{\zeta}$ axis, rather than an entire (normal) plane. In the intermediate cases, where θ_N is neither 0° nor 90°, the ionization channels are therefore mixtures from the Σ_u and Π_u symmetries. This leads to the forbidden plane or line observed in the parallel or perpendicular geometries being smeared out.

Next we examine the effect of the molecular size on the ionization process. Figure 6 shows the ionization probability as a function of the internuclear distance R at two fixed photon energies: $\hbar\omega_0 = 1.50$ and 1.18 a.u. Even for one-photon ionization, the ionization probability shows an unexpected behavior with increasing separation distance. This probability is relatively small at the equilibrium distance of 2.0 bohr. There are two enhanced ionization peaks at smaller and larger separation distances, depending on the photon energy. Since the central photon energies are far less than the ionization

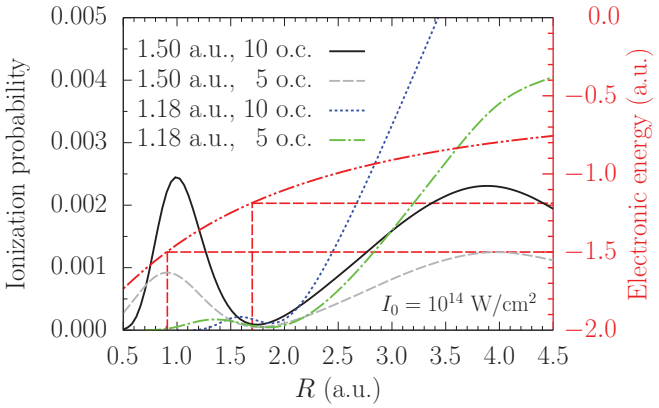

FIG. 6. (Color online) Ionization probabilities (left scale) for H_2^+ in laser pulses at photon energies of 1.50 and 1.18 a.u. for time durations of 10 and 5 cycles. The molecular axis is chosen along the polarization vector. The peak intensity is 10^{14} W/cm^2. The electronic energy (dot-dot-dashed line) versus R is shown on the right scale.

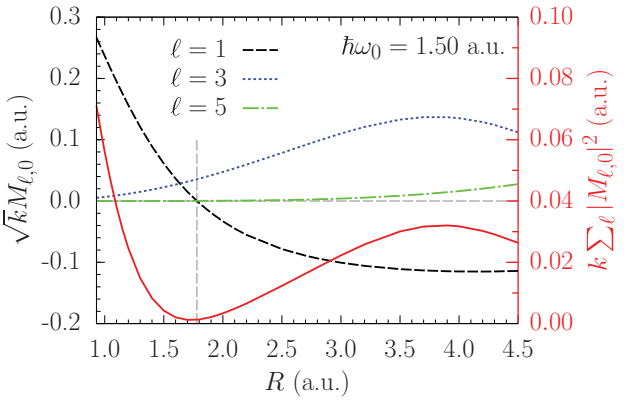

FIG. 7. (Color online) Transition moments (left scale) in the parallel geometry from the channels $\ell = 1$, 3, and 5 at the photon energy of 1.50 a.u. The total squared contribution from all three channels is shown on the right scale (solid curve). The vertical dashed line indicates the R value where $\mathcal{M}_{1,0}$ vanishes.

threshold of 2.0 a.u. in He^+, the ionization probability should be negligibly small in the atomic limit ($R \to 0$). Classically, the ionization channel is open only if $R \gtrsim 0.92$ bohr for $\hbar\omega_0 = 1.50$ a.u., and $R \gtrsim 1.70$ bohr for $\hbar\omega_0 = 1.18$ a.u. Therefore, the opening of the ionization channel is responsible for the peaks observed around 1.0 bohr for the photon energy of 1.50 a.u. and 1.6 bohr for 1.18 a.u. Figure 6 also indicates that the stretched H_2^+ ion has a higher probability to be ionized. This is clearly visible for the photon energy of 1.18 a.u at $R \simeq 4.5$ bohr. Around its equilibrium distance, on the other hand, a minimum develops between these two ionization peaks.

To understand the mechanism behind the suppressed ionization probability at small internuclear separation, consider the dipole transition moment between the initial ground state (Φ_0) and the momentum-normalized continuum state ($\Phi_{\ell,0}^{(k)}$),

$$\mathcal{M}_{\ell,0} = \int d^3\boldsymbol{r}\Phi_{\ell,0}^{(k)*}(\boldsymbol{r})z\Phi_0(\boldsymbol{r}), \tag{36}$$

in the parallel geometry. Here the wave function of the continuum state in the channel ℓ is given by

$$\Phi_{\ell,0}^{(k)}(\boldsymbol{r}) = \frac{1}{k}\Pi_{\ell,0}^{(k)}(\xi)\mathcal{Y}_{\ell,0}(k,\eta,\varphi). \tag{37}$$

The ionization probability at the end of the laser pulse is essentially determined by the sum of the squared transition amplitudes in the ionization channels. Figure 7 depicts the contributions of the transition moments from several channels at the photon energy of 1.50 a.u. Apparently, $\mathcal{M}_{1,0}$ changes sign at $R = 1.78$ bohr, while $\mathcal{M}_{3,0}$ and $\mathcal{M}_{5,0}$ keep their signs in the current region of R between 1.0 and 4.5 bohr. Consequently, the partial-wave cross section in the $(\ell,m) = (1,0)$ channel vanishes at $R = 1.78$ bohr. After taking the contributions from other channels [mostly (3,0)] into account, this results in a double-peak structure with a nonzero minimum at $R \approx 1.78$ bohr in $k\sum_\ell |\mathcal{M}_{\ell,0}|^2$ and, therefore, in the ionization probability.

From the symmetry analysis, the enhanced peak around $R \simeq 1.0$ bohr originates essentially from the spherical component of the Coulomb potential. However, the nonspherical characteristics of the potential in the molecule manifests itself through an enhanced ionization probability from the channel (3,0) at a larger nuclear separation. This shows a strong molecular effect even in single-photon absorption. Overall, the transition moment reproduces fairly well both the positions of the peak and the minimum observed in the ionization probability. Regarding the relative strengths of the two peaks, the ionization probability of Fig. 6 and the transition moment of Fig. 7 are not exactly the same. The two peaks in the ionization probability have nearly the same strength for a 10-cycle pulse, while the transition moment shows a much stronger peak at $R \simeq 1.0$ bohr than at $R \simeq 4.0$ bohr. This difference is related to the pulse length. If the pulse contains more cycles, the peak at $R = 1.0$ bohr is further enhanced in a manner that approaches what is observed in the transition moment.

To get a deeper insight into the sensitivity of the ionization probability to the nuclear separation, we now consider the integrals involved in $\mathcal{M}_{\ell,0}$. The part of the integrand related to the initial state always concentrates in the region near the nuclei, even after integrating over the angular parts. Note that, in the case of a fixed photon energy, a change in R also causes a change in the momentum k of the photoelectron: a larger R yields a larger k. The attractive Coulomb potential pulls the radial diffusive wave functions of the continuum states significantly toward the nuclear region in the present "combination" of R and k, as displayed in Fig. 8 for channel (1,0). With increasing R, therefore, the first negative loop in the continuum-state wave function causes a cancellation of the contribution from the region near the nuclei, thus resulting in a sign change around $R \simeq 1.78$ bohr.

This cancellation effect in the transition moment is similar to the well-known and well-studied Cooper minimum in the photoionization cross sections of some atoms [31]. However, the H_2^+ molecular ion exhibits a noticeable difference compared to the ground states of noble-gas atoms. The sign change in the transition moment only happens in those atoms that have radial nodes in the ground state [e.g., $Ar(3p)^6$], but not in a nodeless ground state [e.g., $Ne(2p)^6$]. This rule of thumb does not hold even for the simplest molecule, as observed

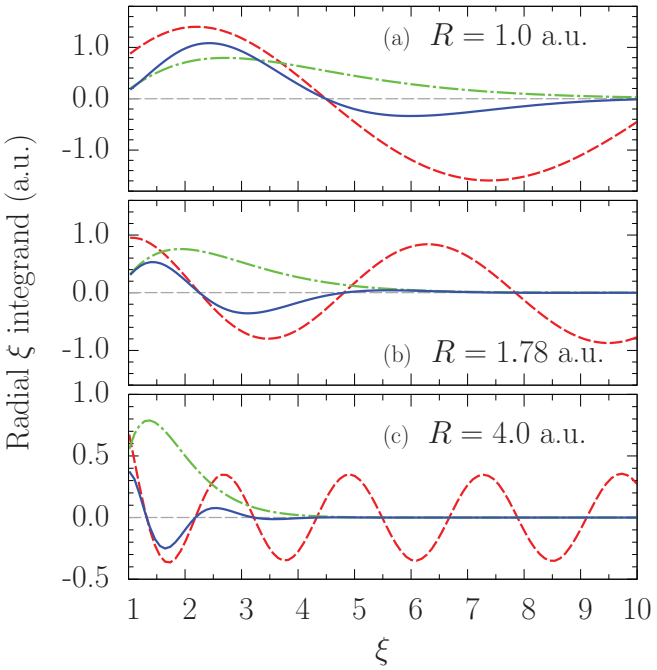

FIG. 8. (Color online) Radial wave functions in the transition moment $\mathcal{M}_{1,0}$. The nuclear separations are (a) 1.0, (b) 1.78, and (c) 4.0 bohr, respectively. The photon energy is 1.5 a.u. Dashed lines: $\xi\Pi_{\ell 0}^{(k)}(\xi)/\sqrt{k}$. Dot-dashed lines: the initial wave function after integrating over the angular part. Solid lines: the product of the dashed and dot-dashed curves. Also note the nonzero values of the wave functions on the left boundary ($\xi = 1$).

here. Although the initial Σ_g^+ ground state of the H_2^+ ion is nodeless, a sign change in the transition moment in the dominant channel is still observed when we vary the nuclear separation. Both constructive or destructive contributions to the transition moments, and therefore the cancellation effect, are sensitive to the detailed overlap between the initial and the continuum states.

The Cooper minimum in the H_2^+ ion is also observable at a fixed equilibrium distance, but only at higher photon energies ($\gtrsim$200 eV) [32]. The suppressed and/or enhanced ionization probabilities discussed here in the FNA could have a far-reaching consequence in the photoionization process [33] when the nuclear motion is simultaneously coupled to the electronic motion in a practical treatment beyond the FNA.

C. Two-photon ionization

Figures 9 and 10 display the total angle-integrated (statistically weighted) two-photon cross section for photon energies from 0.5 to 1.0 a.u. for the parallel geometry and from 0.55 to 1.0 a.u. for the perpendicular geometry, respectively. The present two-photon results are extracted by projecting the time-evolved wave packet onto the continuum states. We use various time scales from 1 fs to 20 fs to compute the cross sections. This may require larger computational grids ($\xi_{\max}$) to fit the electron's temporal motions. For the longest time scale of 20 fs, $\xi_{\max}$ was larger than 1000. With the benefit of prolate spheroidal coordinates and long pulses, it is possible to map out the intermediate-state resonance structure, which was not observed in TDCC predictions [18].

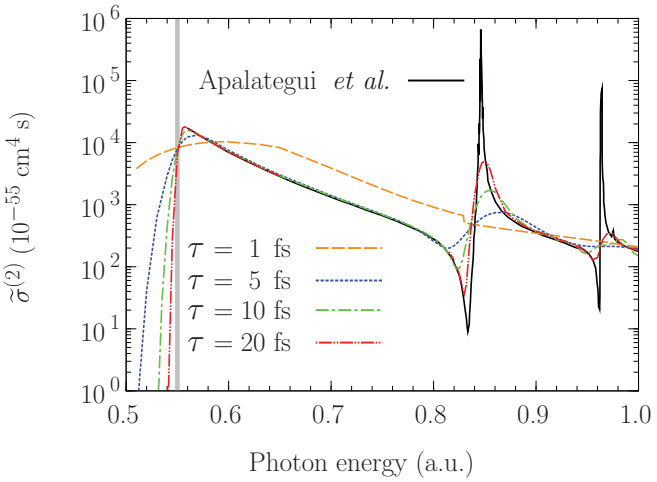

FIG. 9. (Color online) The statistically weighted angle-integrated two-photon cross section [$\tilde{\sigma}^{(2)}$, see Eq. (34)] in the parallel geometry. A sine-squared laser pulse with peak intensity of 10^{13} W/cm^2 was used. The cross section of Apalategui *et al.* [34] obtained in LOPT is also shown (solid line). The threshold for two-photon ionization is indicated by a vertical stripe at the photon energy of 0.55 a.u.

A few features are worth further discussion. First, in the parallel geometry, the shortest pulse of $\sim$1 fs is not sufficient to satisfactorily produce the absolute magnitude of the cross section. Not only are the resonance structures missing, but the calculated total cross sections are far too large even in the nonresonant region; for example, between 0.6 to 0.8 a.u. Results that are directly comparable to steady-state time-independent calculations can only be obtained if the laser pulse lasts at least 5 fs. The cross sections in the nonresonant region are already converged when such a 5 fs pulse is used. With increasing pulse length and hence reduced bandwidth of the photon energies, the resonance peaks and dips narrow and gradually approach the cross sections obtained from the

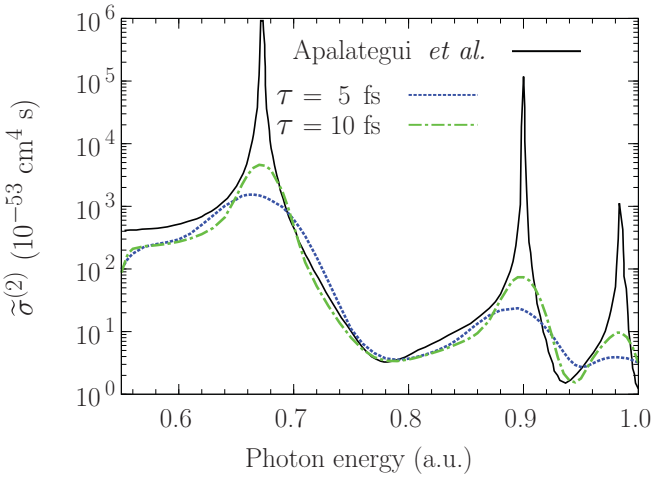

FIG. 10. (Color online) The statistically weighted angle-integrated two-photon cross section [$\tilde{\sigma}^{(2)}$, see Eq. (34)] in the perpendicular geometry. A sine-squared laser pulse with peak intensity of 10^{13} W/cm^2 was used. The cross section of Apalategui *et al.* [34] obtained in LOPT is also shown (solid line).

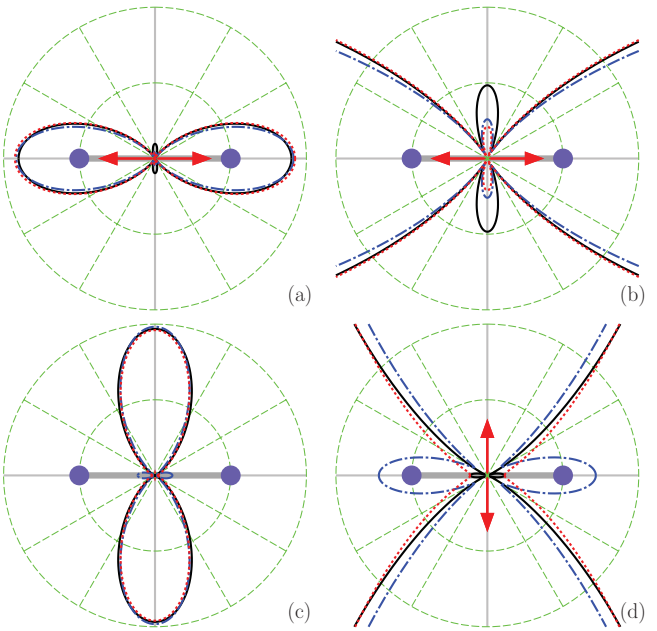

FIG. 11. (Color online) Angular distributions for two-photon ionization of the H_2^+ ion. The time duration of the laser pulse is 10 fs. The panels (a) and (b) are for the parallel geometry at the photon energies of 0.7 (solid), 0.823 (dashed), and 0.854 (dotted) a.u. The panels (c) and (d) are for the perpendicular geometry at the photon energies of 0.674 (solid), 0.8 (dashed), and 0.902 (dotted) a.u. The radii of the outer circles correspond to (a) 2.0×10^{-52}, (b) 0.4×10^{-52}, (c) 1.75×10^{-53}, and (d) 0.28×10^{-53} cm^4 s/sr, respectively. In order to compare the shapes of the curves, the results in the resonance region were multiplied by the sets of scale factors $(f_{0.823}, f_{0.854})$ for panels (a) and (b) and $(f_{0.674}, f_{0.902})$ for panels (c) and (d). These factors were (12.5, 0.75) for (a) and (b) and $(7.0 \times 10^{-4}, 4.3 \times 10^{-2})$ for (c) and (d). Panels (b) and (d) are enlargements of the distributions shown in (a) and (c) near the center. Note the small loop structure perpendicular to the main loop, which for the perpendicular geometry only appears for the photon energy of 0.823 a.u.

time-independent approach, in which the laser field interacts with the target electron practically for an "infinitely" long time.

Second, classically, regardless of the relative orientation, the two-photon ionization channel is only open if the photon energy is larger than 0.55 a.u. For the 1 fs pulse, even at $\hbar\omega_0 = 0.52$ a.u. there is still a noticeable signal of the two-photon ionization. This is due to the large bandwidth of the 1 fs pulse. The uncertainty of $\Delta\omega_0 = 0.26$ a.u. in the photon-energy domain results in possible two-photon ionization. This also explains the observed sharper edge induced by the laser pulses for the longer time scale. The two resonance peaks observed in the current energy regime (cf. Fig. 9) are related to the intermediate one-photon absorption in the manifold of the Σ_u symmetry. The calculated excitation energies from the ground $1s\sigma_g$ state to the second $3p\sigma_u$ and third $4p\sigma_u$ states are 0.847 221 and 0.965 321 a.u., respectively. In the fixed-nuclei approximation, these two intermediate resonance states manifest themselves through enhanced resonance peaks observed in the total cross sections as a function of photon energy. When the photon energy matches the energy gap of 0.435 100 a.u. between the initial $1s\sigma_g$ and the first $2p\sigma_u$ state, an enhanced resonance peak should also be observed. However, it does not correspond to two-photon ionization since the photon energy is below the threshold for two-photon ionization. Instead, it is related to the three-photon ionization process discussed in the next section.

Turning to the perpendicular geometry, only the intermediate π_u states can be detected through two-photon ionization. There are three resonance peaks observed in the photon energy range from 0.55 to 1.0 a.u. Our *ab initio* electronic energies are −0.428 772, −0.200 865, and −0.126 199 a.u., respectively, for the $2p\pi_u$, $3p\pi_u$, and $4f\pi_u$ states. These three states are therefore responsible for the resonance peaks observed at the photon energies of 0.674, 0.902, and 0.976 a.u., respectively. At the same photon energy, the total two-photon cross section in the perpendicular geometry is generally, although not always, larger than the cross section for the parallel geometry.

The H_2^+ ion clearly exhibits different behavior related to the intermediate resonance states with different symmetries. Apparently, both dips and peaks are observed in the parallel geometry (cf. Fig. 9), while only enhanced peaks are seen in the perpendicular geometry (cf. Fig. 10). For very different magnitudes of the total cross sections in the resonance and off-resonance regions, Fig. 11 examines a possible energy dependence of the angular distributions (the shape of the differential cross section) by two-photon absorption at a pulse duration of 10 fs. In the parallel geometry, one of the photon energies chosen is 0.7 a.u. (i.e., far away from resonant regions), while the other two photon energies are 0.823 and 0.854 a.u., respectively, corresponding to a dip and a peak in the resonance region. Three photon energies, 0.674, 0.8, and 0.902 a.u. were chosen for the perpendicular geometry.

The dominant structures in the angular distributions are essentially insensitive to the photon energies. The two-lobe pattern along the direction of laser polarization is the dominant emission mode for both off-resonant and resonant photon energies in both the parallel and perpendicular geometries. Due to the even parity of the two-photon exit channel (Σ_g) in the parallel geometry, however, we observe that ejection of a photoelectron in the normal (to the $\boldsymbol{\epsilon}$ axis) plane is not forbidden anymore, although the cross section is much smaller than in the dominant peaks. Interestingly, the angular distribution at the off-resonance photon energy, $\hbar\omega_0 = 0.7$ a.u., shows a relatively enhanced emission mode in the normal plane, compared with those for resonant photon energies [cf. Fig. 11(b)]. When the light is polarized at right angle with respect to the molecular axis, we observe a similar behavior of the angular distribution at the angle of 90° in the molecular frame: the off-resonance photon energy (0.8 a.u.) shows an enhanced peak compared to the resonant energies [0.674 and 0.902 a.u., cf. Fig. 11(d)].

Recall that the time period of the first vibrational state in H_2^+ is about 15 fs. On the time scale of 10 fs, therefore, the nuclear vibrational motions in the $\Sigma_{g,u}$ states may play a role in modulating the angular distributions of the photoelectron. Based on the calculations of Selstø *et al.* [35] in the parallel geometry, it is not surprising that including the nuclear vibrational motion along the molecular axis does not change the emission mode, except for the enhanced magnitudes of angular distributions. Frozen in its rotational ground state, the nuclear vibrational motion is unrelated to the spatial

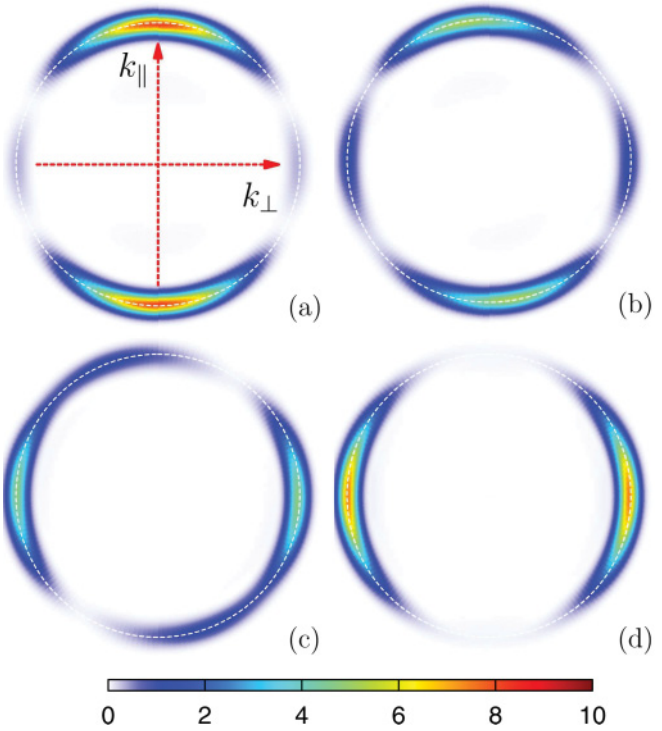

FIG. 12. (Color online) Two-photon ionization probability density $dP_{\rm ion}/d\boldsymbol{k}$ in the $\boldsymbol{\epsilon}$-$\boldsymbol{\zeta}$ plane for various alignment angles θ_N: (a) 0°, (b) 30°, (c) 60°, and (d) 90°. The molecular axis is orientated vertically. $k_\parallel$ and $k_\perp$ are the parallel and perpendicular momentum components, respectively, with respect to the molecular axis. The central photon energy is 0.90 a.u., and the sine-squared pulse with peak intensity of 10^{13} W/cm^2 lasts for 10 optical cycles. The classical momentum is shown as the dashed circle with momentum radius of 1.18 a.u. The linear-scale color bar is given in 10^{-7} per momentum in a.u.

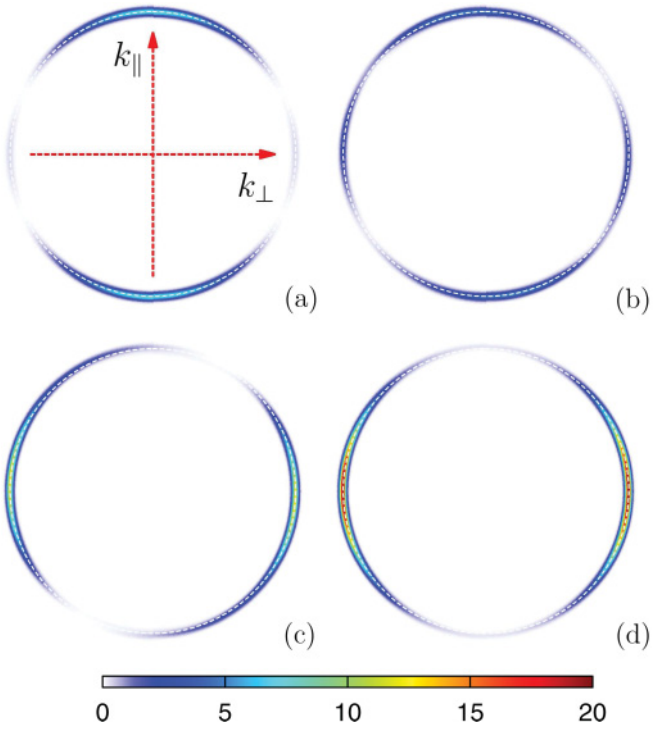

FIG. 13. (Color online) Same as Fig. 12, but the laser pulse lasts for 30 optical cycles. The linear-scale color bar is given in 10^{-6} per momentum in a.u.

symmetry of the photoelectron. In this respect, it is expected that the identical conclusion be valid for other alignment configurations. Observation of photoelectron emission in the normal plane is in qualitative agreement with the prediction of Ref. [35]. In contrast, these emission patterns at the angle of 90° are negligibly small in both the parallel and perpendicular geometries in Ref. [20].

Figures 12 and 13 depict the ionization-probability density for two-photon absorption, $dP_{\rm ion}/d\boldsymbol{k}$, in momentum space. If the pulse duration is sufficiently short (e.g., 10 cycles), the parallel geometry may have a similar or even larger ionization probability than the perpendicular case. However, the situation changes when the H_2^+ ion is exposed to a laser field with a longer interaction time, as shown for the case of a 0.90 a.u. (24.5 eV) photon energy in Fig. 13. Longer pulses and weak fields are apparently needed to approach converged cross sections. The aligned H_2^+ ion shows a sensitive response to laser pulses with respect to the time duration. This illustrates the alignment effect. The time-duration effect of the laser pulse clearly manifests itself through the alignment of the diatomic molecular axis with respect to the polarization direction.

D. Three-photon ionization

Figure 14 shows the total cross section (unweighted) for three-photon absorption for photon energies from 0.35 to 0.5 a.u. Again, the results are compared with the predictions of time-independent perturbation theory [22]. We converted the angle-integrated cross sections given in units of cm^6/W^2 from Ref. [22] to the units of cm^{6}s^2 through $\sigma^{(3)}$ (cm^{6}s^2) = $1.9 \times 10^{-35}\sigma^{(3)}$ (cm^6/W^2) for three-photon ionization.

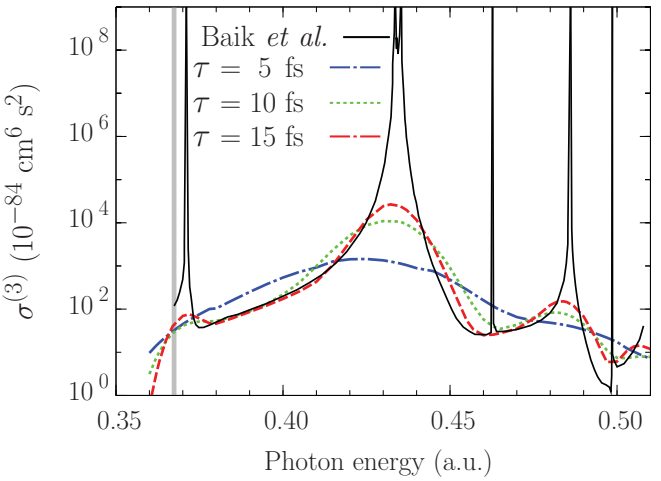

FIG. 14. (Color online) Angle-integrated three-photon cross section [$\sigma^{(3)}$, no statistical factor was multiplied] in the parallel geometry for a number of different pulse lengths. The peak intensity of the sine-squared pulse is 10^{13} W/cm^2. The cross sections of Baik *et al.* [22] obtained in LOPT are also shown (solid line).

The channel of three-photon ionization is open if $\hbar\omega_0 \geqslant 0.37$ a.u. In the time-dependent treatment, the very narrow resonance peak around 0.37 a.u. near the threshold can only be identified when using a long pulse (at least 15 fs), while the resonance peaks at 0.46 and 0.50 a.u. are not observable on the present time scale. Clearly, the three-photon ionization process shows an even more complicated resonance behavior than the two-photon case. The first peak at a photon energy of 0.37 a.u. corresponds to a two-photon-intermediate resonance in three-photon ionization. Since the energy of the first-excited $2s\sigma_g$ state is $-0.360\,87$ a.u., two-photon absorption at 0.37 a.u. hits the $2s\sigma_g$ state and therefore causes the system to be resonantly populated in this state. Similarly, for the peak at 0.486 a.u., the intermediate $4d\sigma_g$ state is resonantly excited first and then ionized by subsequent two-photon absorption.

At the photon energy of 0.435 a.u., however, the resonance peak is due to a combination of contributions from two ionization paths. A photon of energy 0.435 a.u. can hit the excited $2p\sigma_u$ state, and then ionization happens after another two-photon absorption. At the same time, the system can also be excited to the $3d\sigma_g$ state by two-photon absorption before being ionized after absorbing one more photon. These two paths add coherently, and they manifest themselves as an overlap, resulting in a single but wider than usual resonance peak in the cross section.

V. SUMMARY AND OUTLOOK

As an initial step to develop a fully *ab initio*, nonperturbative computational approach to understand the intricate molecular response to temporal laser fields from ultrafast attosecond to femtosecond time scales, we investigated the one-, two-, and three-photon ionization of the hydrogen molecular ion in the fixed-nuclei approximation. The current situation regarding the published DCS results for one-photon ionization was clarified and updated. Accurate benchmark results for the angle-resolved differential cross sections have therefore been established for the H_2^+ molecular ion.

For one-photon ionization, a reduction in the ionization probability was observed at a specific internuclear separation distance—in fact, near the equilibrium distance. This result can be explained as a consequence of the transition amplitude in the dominant ionization channel changing its sign. This is the same mechanism that causes the Cooper minima observed in photoionization of some atoms. Resonance-enhanced peaks in the angle-integrated cross sections for two- and three-photon ionization were also analyzed.

While the effect of nuclear motion was neglected in the present work, we are currently working on a program to include the nuclear degree of freedom into our *ab initio* treatment of the molecular dynamics, both adiabatically and nonadiabatically. In addition to the electron coordinates, discretizing the entire problem including the nuclear separation, or expansion in terms of potential energy curves in the Born-Oppenheimer approximation, promise an elaborate depiction of twisted motions on a varying time scale. As discussed previously [36], effects of the nuclear motion already show some signals even in one- or two-photon ionization. The Cooper-type minimum should also have a significant influence on the angular distributions. While beyond the scope of the present work, we plan to study this is more detail in the future, since it would need to be accounted for in calculations with variable internuclear distance.

Most importantly, the nuclear motion could dramatically affect observable quantities, such as the spectra for above-threshold ionization in infrared laser fields on a femtosecond time scale [37]. Incorporating the nuclear motion *ab initio* will allow us to analyze the experimental spectra of dissociative kinetic-energy release in H_2^+ and D_2^+ [38], which have not yet been explained in a satisfactory way by models with reduced dimensions. Including the effect of moving nuclei even in the simplest H_2^+ molecule might also shed additional light on the more complicated double-photoionization process in H_2.

ACKNOWLEDGMENTS

This work was supported by the NSF under Grant No. PHY-0757755 (XG and KB). We thank Dr. J. Colgan for clarifying how the DCSs in Refs. [14,15] were defined and Dr. Della Picca for sending us her data in numerical form.

[1] E. A. Hylleraas, Z. Phys. **71**, 739 (1931).
[2] J. D. Power, Phil. Trans. Roy. Soc. London A **274**, 663 (1973).
[3] M. M. Madsen and J. M. Peek, Atomic Data **2**, 171 (1971).
[4] B. Fischer, M. Kremer, T. Pfeifer, B. Feuerstein, V. Sharma, U. Thumm, C. D. Schröter, R. Moshammer, and J. Ullrich, Phys. Rev. Lett. **105**, 223001 (2010).
[5] K. P. Singh *et al.*, Phys. Rev. Lett. **104**, 023001 (2010).
[6] A. Picón, A. Bahabad, H. C. Kapteyn, M. M. Murnane, and A. Becker, Phys. Rev. A **83**, 013414 (2011).
[7] K.-J. Yuan, H. Z. Lu, and A. D. Bandrauk, Phys. Rev. A **83**, 043418 (2011).
[8] J. Fernández, F. L. Yip, T. N. Rescigno, C. W. McCurdy, and F. Martín, Phys. Rev. A **79**, 043409 (2009).
[9] V. Roudnev, B. D. Esry, and I. Ben Itzhak, Phys. Rev. Lett. **93**, 163601 (2004).
[10] J. McKenna *et al.*, Phys. Rev. Lett. **100**, 133001 (2008).
[11] P. A. Orr, I. D. Williams, J. B. Greenwood, I. C. E. Turcu, W. A. Bryan, J. Pedregosa-Gutierrez, and C. W. Walter, Phys. Rev. Lett. **98**, 163001 (2007).
[12] E. Dehghanian, A. D. Bandrauk, and G. L. Kamta, Phys. Rev. A **81**, 061403 (2010).
[13] Y. V. Vanne and A. Saenz, Phys. Rev. A **82**, 011403 (2010).
[14] M. Foster, J. Colgan, O. Al-Hagan, J. L. Peacher, D. H. Madison, and M. S. Pindzola, Phys. Rev. A **75**, 062707 (2007); J. Colgan (private communication).
[15] J. Colgan, A. Huetz, T. J. Reddish, and M. S. Pindzola, J. Phys. B **41**, 085202 (2008).
[16] T. N. Rescigno, D. A. Horner, F. L. Yip, and C. W. McCurdy, Phys. Rev. A **72**, 052709 (2005).

[17] L. Tao, C. W. McCurdy, and T. N. Rescigno, Phys. Rev. A **79**, 012719 (2009).
[18] J. Colgan, M. S. Pindzola, and F. Robicheaux, Phys. Rev. A **68**, 063413 (2003).
[19] M. Plummer and J. F. McCann, J. Phys. B **28**, 4073 (1995).
[20] L. Tao, C. W. McCurdy, and T. N. Rescigno, Phys. Rev. A **80**, 013402 (2009).
[21] S. X. Hu, L. A. Collins, and B. I. Schneider, Phys. Rev. A **80**, 023426 (2009).
[22] M.-G. Baik, M. Pont, and R. Shakeshaft, Phys. Rev. A **54**, 1570 (1996).
[23] X. Guan, K. Bartschat, and B. I. Schneider, Phys. Rev. A **83**, 043403 (2011).
[24] X. Guan, C. J. Noble, O. Zatsarinny, K. Bartschat, and B. I. Schneider, Comput. Phys. Commun. **180**, 2401 (2009).
[25] X. Guan and K. Bartschat, Phys. Rev. Lett. **103**, 213201 (2009).
[26] L. B. Madsen, L. A. A. Nikolopoulos, and P. Lambropoulos, Eur. Phys. J. D **10**, 67 (2000).
[27] J. Colgan, M. S. Pindzola, and F. Robicheaux, Phys. Rev. Lett. **98**, 153001 (2007).
[28] L. A. A. Nikolopoulos, T. K. Kjeldsen, and L. B. Madsen, Phys. Rev. A **76**, 033402 (2007).
[29] R. Della Picca, P. D. Fainstein, M. L. Martiarena, and A. Dubois, J. Phys. Conf. Ser. **141**, 012006 (2008).
[30] R. Della Picca (private communication).
[31] A. F. Starace, in *Handbuch der Physik*, edited by W. Mehlhorn (Springer-Verlag, Berlin, 1982), Vol. 31, p. 1.
[32] R. Della Picca, P. D. Fainstein, M. L. Martiarena, and A. Dubois, Phys. Rev. A **77**, 022702 (2008).
[33] S. Barmaki, S. Laulan, H. Bachau, and M. Ghalim, J. Phys. B **36**, 817 (2003).
[34] A. Apalategui, A. Saenz, and P. Lambropoulos, J. Phys. B **33**, 2791 (2000).
[35] S. Selstø, A. Palacios, J. Fernández, and F. Martin, Phys. Rev. A **75**, 033419 (2007).
[36] A. Palacios, S. Barmaki, H. Bachau, and F. Martín, Phys. Rev. A **71**, 063405 (2005).
[37] A. D. Bandrauk, S. Chelkowski, and I. Kawata, Phys. Rev. A **67**, 013407 (2003).
[38] S. Chelkowski, A. D. Bandrauk, A. Staudte, and P. B. Corkum, Phys. Rev. A **76**, 013405 (2007).